Nano Research

Open Access

Research Article

Dual-functional 2-mercaptopyridine-N-oxide doping for simultaneous electronic optimization and silver electrode stabilization in inverted perovskite solar cells

Ziyu Wang[1] ✉, Zhiqing Liang[1], Ling Li[1], Bo Zhang[1], Mengyuan Li[1], Dong Yang[2] ✉, and Yanlin Song[3] ✉

[1] College of Chemistry and Pingyuan Laboratory, Zhengzhou University, Zhengzhou 450001, China
[2] State Key Laboratory of Photoelectric Conversion and Utilization of Solar Energy, Dalian Institute of Chemical Physics, Chinese Academy of Sciences, Dalian 116023, China
[3] Key Laboratory of Green Printing, Institute of Chemistry, Chinese Academy of Sciences (ICCAS), Beijing Engineering Research Center of Nanomaterials for Green Printing Technology, National Laboratory for Molecular Sciences (BNLMS), Beijing 100190, China

Cite this article: *Nano Research*, **2026**, *19*, 94908437. https://doi.org/10.26599/NR.2026.94908437

ABSTRACT: Simultaneously addressing nanoscale interfacial charge transport inefficiency and Ag electrode diffusion remains a critical bottleneck for scalable inverted perovskite solar cells (PSCs). Herein, we report a dual-functional molecular engineering strategy by doping 2-mercaptopyridine-N-oxide (2-MPNO) into the 10 nm-thick nanoscale bathocuproine (BCP) cathode buffer layer, achieving synergistic optimization of interfacial energy alignment and Ag^+ diffusion inhibition. The n-type doping effect of 2-MPNO triples the electron mobility of the [6,6]-phenyl-C61-butyric acid methyl ester (PCBM)/BCP layer (via space-charge-limited current measurements), with ultraviolet photoelectron spectroscopy confirming a 0.37 eV upward Fermi level shift to optimize nanoscale interfacial energy alignment. Owing to the incomplete coverage of PCBM on the perovskite surface, 2-MPNO molecules infiltrate the perovskite interface, effectively passivating defects and reducing non-radiative recombination. Concurrently, the –SH and N–O groups of 2-MPNO form bidentate coordination with Ag at the nanoscale Ag/BCP interface, constructing a molecular barrier to block Ag^+ migration. As a result, the optimized device exhibits an improvement in efficiency from 23.56% to 25.31%. More importantly, unencapsulated devices maintain 97.4% of their original efficiency after 2115 h stored in air with a relative humidity of 15% ± 5% and retain 94.0% of their initial efficiency following thermal aging at 65 °C for 1256 h in a nitrogen environment.

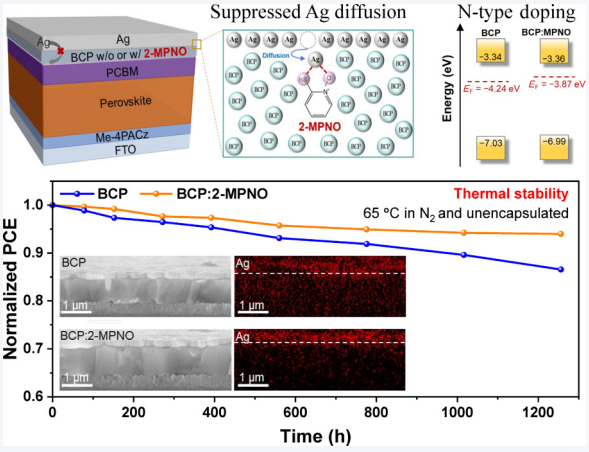

KEYWORDS: perovskite solar cells, cathode buffer layer, n-type doping, bidentate coordination, silver electrode stabilization

1 Introduction

Inverted (p-i-n) perovskite solar cells (PSCs), with certified efficiency exceeding 27% to date [1, 2], have emerged as a prominent third-generation photovoltaic technology owning to their low-temperature fabrication (< 150 °C), minimal current-voltage hysteresis, and compatibility with silicon-based integration for achieving extremely high efficiencies [3–5]. However, challenges including charge transfer degradation at the cathode interface during prolonged air exposure and metal diffusion issues remain major obstacles to their commercial viability [6, 7].

As a commonly-used electron transport material, [6,6]-phenyl-C61-butyric acid methyl ester (PCBM) offers high electron mobility but suffers three main drawbacks at the interface with metal electrodes (e.g. Ag): (i) The high work function of the metal electrodes induces charge diffusion, leading to upward energy level bending and Schottky barrier formation, which hinder electron extraction [8]; (ii) the incomplete coverage of PCBM film [9] often produces pinholes that permit direct contact between the perovskite layer and metal electrode, thereby accelerating halide ion (I^-/Br^-)

Received: November 20, 2025; **Revised:** January 7, 2026
Accepted: January 13, 2026

✉Address correspondence to Ziyu Wang, zywang@zzu.edu.cn; Dong Yang, dongyang@dicp.ac.cn; Yanlin Song, ylsong@iccas.ac.cn

migration, electrochemical corrosion of silver electrodes and formation of insulating compounds like silver iodide (AgI) [10, 11]; (iii) Ag^+ ions can diffuse along grain boundaries into the perovskite during operation, creating deep-level defects (e.g., Ag interstitials) that destabilize the perovskite lattice and lead to irreversible device degradation [12, 13].

To address these issues, researchers have explored various interface strategies via introducing an interface buffer layer, between PCBM electron transport layer (ETL) and the metal electrode [14–17]. Existing strategies for nanoscale interface modification face trade-offs: atomic layer deposition (ALD)-fabricated ultrathin Al_2O_3/TiO_2 nanolayers block Ag^+ diffusion but increase series resistance, lowering the fill factor (FF) [18, 19]; $Zr(Ac)_4$ forms uniform, dense films on PCBM that improve interface contact but fail to suppress metal diffusion [20, 21]. Therefore, the choice of materials for the ideal cathode buffer layer should meet requirements that facilitate charge extraction and block ion penetration. Strategies involving coordination chemistry have been employed as promising alternatives. Liu et al. employed 2-mercaptobenzothiazole (MBT) to strongly coordinate with Ag, effectively enhancing the device stability under humid conditions [22]. Chen et al. enhanced copper electrode corrosion resistance through benzimidazole (BTA) complexation, significantly boosting thermal stability [23]; Yang and Li et al. respectively incorporated the heavy metal chelating agent 1,3,5-triazine-2,4,6-trithiol trisodium salt (TTTS) [24] and the ionic liquids 1-ethyl-3-methylimidazolium-2-mercaptobenzothiazole (EM) [25] into bathocuproine (BCP) to coordinate with metal electrodes, suppressing chemical reactions and corrosion at the perovskite/electrode interface. These findings highlight the potential of bi-functional molecules as cathode buffer layers for enhancing interface stability.

In this work, we adopt a molecular doping approach by incorporating 2-mercaptopyridine-N-oxide (2-MPNO) into the BCP buffer layer to synergistically enhance interfacial charge transfer and chemical stability. The distinctive electronic structure of 2-MPNO enables a dual-function mechanism: (i) The pyridine N–O group acts as a strong electron donor, increasing BCP's conductivity via n-type doping and optimizing interfacial energy level alignment (with a Fermi level shift upward by 0.37 eV); (ii) the thiol (–SH) and N–O groups create bidentate coordination sites that strongly bind to Ag atoms, forming an ion diffusion barrier. Experimental findings further demonstrate that 2-MPNO infiltrates through PCBM pinholes to passivate perovskite surface defects [26], while concurrently establishing a molecular-level barrier at the Ag/BCP interface. As a result, the optimized device achieves a power conversion efficiency (PCE) of 25.31%, retaining 94.0% of its initial efficiency after accelerated aging at 65 °C for 1256 h, with a degradation rate 2.2 times slower than that of the control device. These enhancements are attributed to the bi-functional molecule that serves as a molecular bridge between the ETL and Ag electrode. Our work thus provides a promising strategy for interface engineering toward stable, mass-producible PSCs for real-world applications.

2 Experimental

2.1 Materials

Patterned fluorine-doped tin oxide (FTO) substrates, lead iodide (PbI_2, 99.999%), formamidinium iodide (FAI, 99.5%), methylamine hydrochloride (MACl, 99.5%), cesium iodide (CsI, 99.999%), lead bromide ($PbBr_2$, 99.99%), methylammonium bromide (MABr, 99.9%), PCBM (99.9%), and bathocuproine (BCP, >99.0%) were purchased from Advanced Election Technology Co., Ltd. [4-(3,6-Dimethyl-9H-carbazol-9-yl)butyl]phosphonic acid (Me-4PACz, 99%) was purchased from Tokyo Chemical Industry Co., Ltd. Ethyl acetate (EA, 99.9%), chlorobenzene (CB, 99.9%), isopropyl alcohol (IPA, 99.5%), N,N-dimethylformamide (DMF, 99.5%), and dimethyl sulfoxide (DMSO, 99.9%) were purchased from Alfa Aesar. 2-MPNO (98%) was purchased from Admas.

2.2 Device fabrication

FTO glass substrates were sequentially ultrasonicated in detergent, deionized water, acetone, and isopropanol, dried under N_2 flow, and ultraviolet (UV)-ozone treated for 15 min. The cleaned substrates were transferred to a nitrogen-filled glovebox for subsequent processing. Me-4PACz solution (0.5 mg/mL in IPA) was spin-coated at 3000 rpm for 30 s, followed by annealing at 100 °C for 10 min. The 1.5 M perovskite precursor solution with a composition of $Cs_{0.05}(FA_{0.98}MA_{0.02})_{0.95}Pb(I_{0.99}Br_{0.01})_3$ with 5 mol% excess PbI_2 and 10 mol% MACl additive was prepared by dissolving CsI, FAI, PbI_2, MABr, $PbBr_2$, and MACl (molar ratio 0.05:0.93:1.04:0.02:0.01:0.10) in DMF:DMSO (4:1 v/v). The solution was spin-coated in two stages: first, 1000 rpm for 10 s (spread step); then, 4000 rpm for 40 s (acceleration step) with 150 μL ethyl acetate anti-solvent dripped at 15 s before completion. The resulting film (650 nm) was annealed at 100 °C for 30 min. Subsequently, the PCBM solution (20 mg/mL in CB) was spin-coated onto the perovskite film at 4000 rpm for 30 s to obtain a PCBM layer (60 nm). The BCP:2-MPNO solution (mix BCP solution (0.5 mg/mL in IPA) and 2-MPNO solution (0.5 mg/mL in IPA) in volume ratios of 1:10, 1:15, and 1:20 respectively) was then spin coated onto the PCBM film at 4000 rpm for 30 s to obtain 10 nm-thick buffer layers. Finally, 100 nm of Ag was deposited as an electrode by thermal evaporation using a shadow mask (0.04 cm^2).

2.3 Characterization

Solar cell performance was evaluated through current density–voltage (*J–V*) analysis under simulated AM 1.5G illumination (100 mW/cm^2) using a solar simulator (SS-X50, Enlitech) coupled with a Keithley B2901A precision source meter. Optical characterization involved photoluminescence (PL) and time-resolved PL (TRPL) spectroscopy utilizing a HORIBA FluoroMax fluorescence spectrometer equipped with pulsed excitation capabilities. For carrier dynamics studies, transient photocurrent (TPC) and photovoltage (TPV) decay profiles were acquired using a PAIOS characterization platform (Fluxim), which also enabled space-charge-limited current (SCLC) mobility analysis. Spectral response measurements were performed with a quantum efficiency system (QE-R, Enlitech) under monochromatic illumination conditions. Material optical properties were investigated via ultraviolet–visible (UV–Vis) absorption spectroscopy using an Agilent Cary 5000 spectrophotometer. Morphological examination employed scanning electron microscopy (SEM) with a Hitachi Regulus 8100 system operating at high-vacuum conditions. Surface electronic structure analysis combined X-ray photoelectron spectroscopy (XPS) measurements using a Thermo Scientific K-Alpha system and ultraviolet photoelectron spectroscopy (UPS) with a Thermo Scientific Escalab Xi+ spectrometer to determine valence band maxima and work functions.

3 Results and discussion

3.1 Device architecture and photovoltaic performance

The devices utilize an inverted (p-i-n) planar configuration (Fig. 1(a)), featuring a modified cathode buffer layer created by blending 2-MPNO with BCP (referred to as BCP:2-MPNO). Device performance was optimized by adjusting the doping concentration of 2-MPNO in BCP (Fig. S1 in the Electronic Supplementary Material (ESM)). As the mass ratio of 2-MPNO to BCP increased from 1:20 to 1:10, the efficiency initially rose and then declined, peaking at a 1:15 ratio. Detailed photovoltaic parameters are provided in Table S1 in the ESM. Notably, the device efficiency showed relatively low sensitivity to the doping ratio of 2-MPNO. Figure 1(b) illustrates the molecular structure of 2-MPNO, which is a product of cleavage of the disulfide bond in 2,2'-dithiobis(pyridine-N-oxide). It retains sulfur and oxygen functional groups capable of coordination and exhibits excellent solubility in isopropanol. This allows for uniform blending with BCP while preserving the metal corrosion-inhibiting properties of the parent molecule.

The effect of 2-MPNO on device performance was assessed through current density–voltage (J–V) measurements (Fig. 1(c)). Compared to devices using pure BCP, the optimized BCP:2-MPNO devices demonstrated notable improvements: PCE increased from 23.56% (reverse scan) to 25.31%, V_{OC} from 1.112 to 1.157 V, J_{SC} from 25.77 to 26.05 mA/cm^2, and FF from 82.23% to 83.92%. Additionally, the hysteresis index (HI) decreased from 2.0% to 1.2%. These enhancements are attributed to 2-MPNO's ability to optimize interfacial contact, facilitating charge transfer and reducing recombination at the interface [27].

To confirm reproducibility, photovoltaic parameters were statistically analyzed across 20 independent devices (Fig. 1(d) and Fig. S2 in the ESM). Detailed performance parameters are summarized in Tables S2 and S3 in the ESM. Devices with BCP:2-MPNO showed more consistent distributions of V_{OC} (1.153 ± 0.003 V), J_{SC} (26.02 ± 0.05 mA/cm^2), FF (83.66% ± 0.31%), and PCE (25.12% ± 0.12%), outperforming the control group (V_{OC}: 1.115 ± 0.004 V, J_{SC}: 25.76 ± 0.11 mA/cm^2, FF: 80.79% ± 1.00%, PCE: 23.21% ± 0.30%), indicating excellent reliability and repeatability of this approach. External quantum efficiency (EQE) measurements further validated the performance enhancement (Fig. 1(e)). The BCP:2-MPNO devices exhibited a slightly higher spectral response between 300 and 800 nm, with an integrated photocurrent density of 25.30 mA/cm^2, consistent with J–V data. Steady-state power output (SPO) tests (Fig. 1(f)) revealed that the optimized device maintained a power output of 25.01% at 1.02 V bias, significantly surpassing the control device of 22.61% at 0.98 V, demonstrating stable operation under practical conditions.

3.2 Film characterization of 2-MPNO doped BCP

SEM images (Figs. 2(a) and 2(b)) and atomic force microscopy (AFM) images (Fig. S3 in the ESM) demonstrate that doping BCP films with 2-MPNO greatly enhances their morphology, producing a denser and more uniform surface. To assess electrical properties, devices with the structure ITO/Ag/PCBM/BCP:2-MPNO (or BCP)/Ag were fabricated, and electron mobility was measured using the SCLC method [28]. As illustrated in Fig. 2(c), adding 2-MPNO increased the electron mobility of the PCBM/BCP layer by two times, indicating a notable improvement in charge transport at the interface. This result also indicates that the introduction of 2-MPNO has increased the electrical conductivity of BCP. To verify that the enhanced conductivity originates from the N-oxide moiety rather than the entire molecular backbone, a control experiment was performed by doping 2-mercaptopyridine (2-MP) into BCP for electron mobility measurements. The experimental results are shown in Fig. S4 in the ESM. The PCBM/BCP:2-MP layer exhibits an electron mobility comparable to that of PCBM/BCP, indicating that the conductivity enhancement of BCP:2-MPNO mainly arises from the N-oxide moiety.

To investigate changes in energy levels, UPS was conducted on BCP films before and after doping with 2-MPNO (Fig. 2(d)). The bandgap was determined from Tauc plots based on absorption

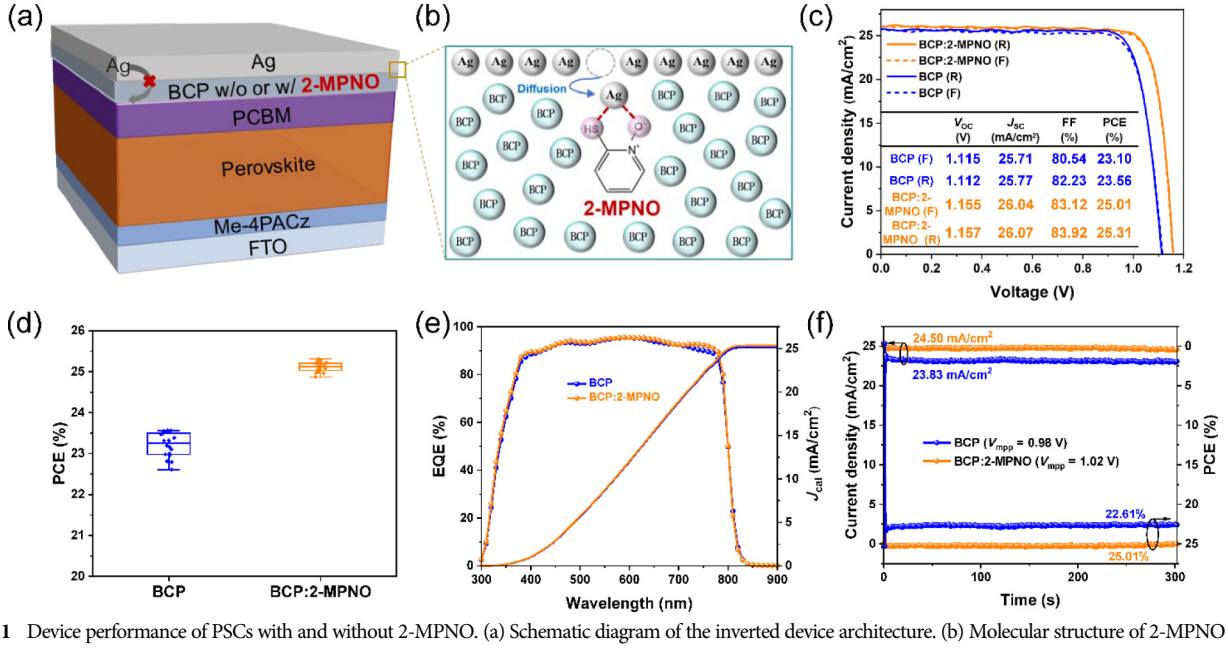

	V_{OC} (V)	J_{SC} (mA/cm²)	FF (%)	PCE (%)
BCP (F)	1.115	25.71	80.54	23.10
BCP (R)	1.112	25.77	82.23	23.56
BCP:2-MPNO (F)	1.155	26.04	83.12	25.01
BCP:2-MPNO (R)	1.157	26.07	83.92	25.31

Figure 1 Device performance of PSCs with and without 2-MPNO. (a) Schematic diagram of the inverted device architecture. (b) Molecular structure of 2-MPNO and its interaction with Ag electrode. (c) Forward and reverse J–V curves. (d) Statistical distribution of PCE for 20 devices. (e) EQE spectra. (f) Steady-state power output under bias.

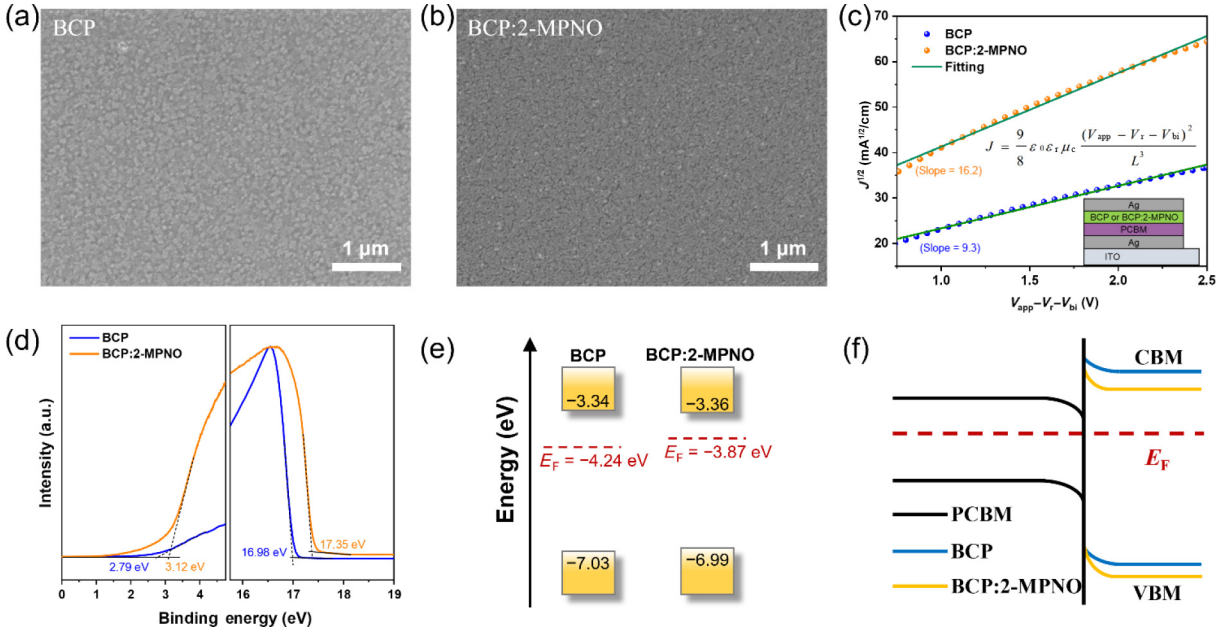

Figure 2 Effects of 2-MPNO doping on BCP films. SEM images of (a) BCP and (b) BCP:2-MPNO films. (c) Electron mobility for PCBM/BCP and PCBM/BCP:2-MPNO using the SCLC model, and the inset shows the device structure of ITO/Ag/PCBM/BCP or BCP:2-MPNO/Ag. (d) UPS spectra and (e) electronic energy level diagram of BCP and BCP:2-MPNO films. (f) Energy band diagram of BCP or BCP:2-MPNO layer contacting PCBM layer.

spectra (Fig. S5 in the ESM). Doping caused the Fermi level to shift upward by 0.37 eV, demonstrating effective n-type doping, while the valence band maximum (VBM) and conduction band minimum (CBM) remained mostly unchanged (Figs. 2(e) and 2(f)). Analysis of energy level alignment reveals that doping lowers the electron extraction barrier by reducing the conduction band offset with PCBM, which aligns with the observed increase in SCLC mobility and promotes more efficient charge transfer across the interface.

3.3 Interfacial charge extraction and recombination dynamics

The effect of BCP:2-MPNO on charge separation at the perovskite/ETL interface was examined using steady-state and time-resolved photoluminescence (PL/TRPL) (Figs. 3(a) and 3(b)). Devices doped with 2-MPNO showed a reduction in PL intensity to 37% of the control, suggesting improved charge extraction efficiency. TRPL measurements revealed that the average carrier lifetime decreased from 52.7 to 31.0 ns (Table S4 in the ESM), further supporting enhanced interfacial charge transfer. TPV and TPC analyses (Figs. 3(c) and 3(d)) demonstrated that devices containing 2-MPNO exhibited slower voltage decay and faster current decay, respectively, indicating suppressed non-radiative recombination and enhanced charge extraction [29]. Additionally, electroluminescence (EL) intensity (Fig. 3(e)) was markedly increased, consistent with decreased recombination losses [30].

Trap-assisted recombination was investigated by determining the ideality factor (n) from the relationship between V_{OC} and light intensity (Fig. 3(f)) [31]. The BCP:2-MPNO device exhibited a lower ideality factor (1.15) compared to the control device (1.31), indicating a reduction in trap-related recombination [32]. Furthermore, trap density (N_{trap}) was assessed via SCLC measurements. Electron-only devices with the configuration FTO/SnO_2/perovskite/PCBM/BCP:2-MPNO (or BCP)/Ag were fabricated, and their J–V characteristics were recorded in the dark. As depicted in Fig. 3(g), the trap-filled limit voltage (V_{TFL}) for the BCP:2-MPNO device was 0.41 V, which is lower than the 0.68 V observed for the BCP device. The N_{trap} can be calculated using Eq. (1) [33]

$$N_{trap} = \frac{2\varepsilon_0\varepsilon_r}{eL^2} V_{TFL} \quad (1)$$

where ε_0 is the vacuum permittivity, ε_r is the relative permittivity of the perovskite film, e is the elementary charge, and L is the thickness of the perovskite layer (~ 650 nm). The N_{trap} values for BCP:2-MPNO and BCP devices were calculated to be 3.09×10^{15} and 5.12×10^{15} cm^{-3}, respectively. This result indicates that the incorporation of 2-MPNO reduces internal defects in the device, thereby enhancing charge transport capability. This defect reduction is likely associated with the penetration of 2-MPNO through pinholes in the PCBM layer to reach the perovskite surface, where it can interact with and passivate surface defects. To substantiate this mechanism, devices with the configuration ITO/perovskite/PCBM/BCP:2-MPNO were fabricated and characterized by time-of-flight secondary ion mass spectrometry (TOF-SIMS) depth profiling. As shown in Fig. S6 in the ESM, a clear enrichment of 2-MPNO at the Perovskite/PCBM interface is observed, providing direct evidence that 2-MPNO infiltrates through PCBM pinholes and passivates the perovskite surface.

Capacitance–voltage (C–V) measurements and electrochemical impedance spectroscopy (EIS) analyses were conducted on the devices under dark conditions. As illustrated in the Mott–Schottky plot presented in Fig. 3(h), the built-in potential (V_{bi}) of the BCP device was determined to be 0.96 eV, which increased to 1.01 eV following doping with 2-MPNO. This increase suggests that the incorporation of 2-MPNO enhanced charge carrier extraction and transfer at the interface, thereby mitigating interfacial charge accumulation and recombination, and consequently improving the V_{OC} of the device [34]. The EIS data, shown in Fig. 3(i) along with the corresponding equivalent circuit model, were fitted with

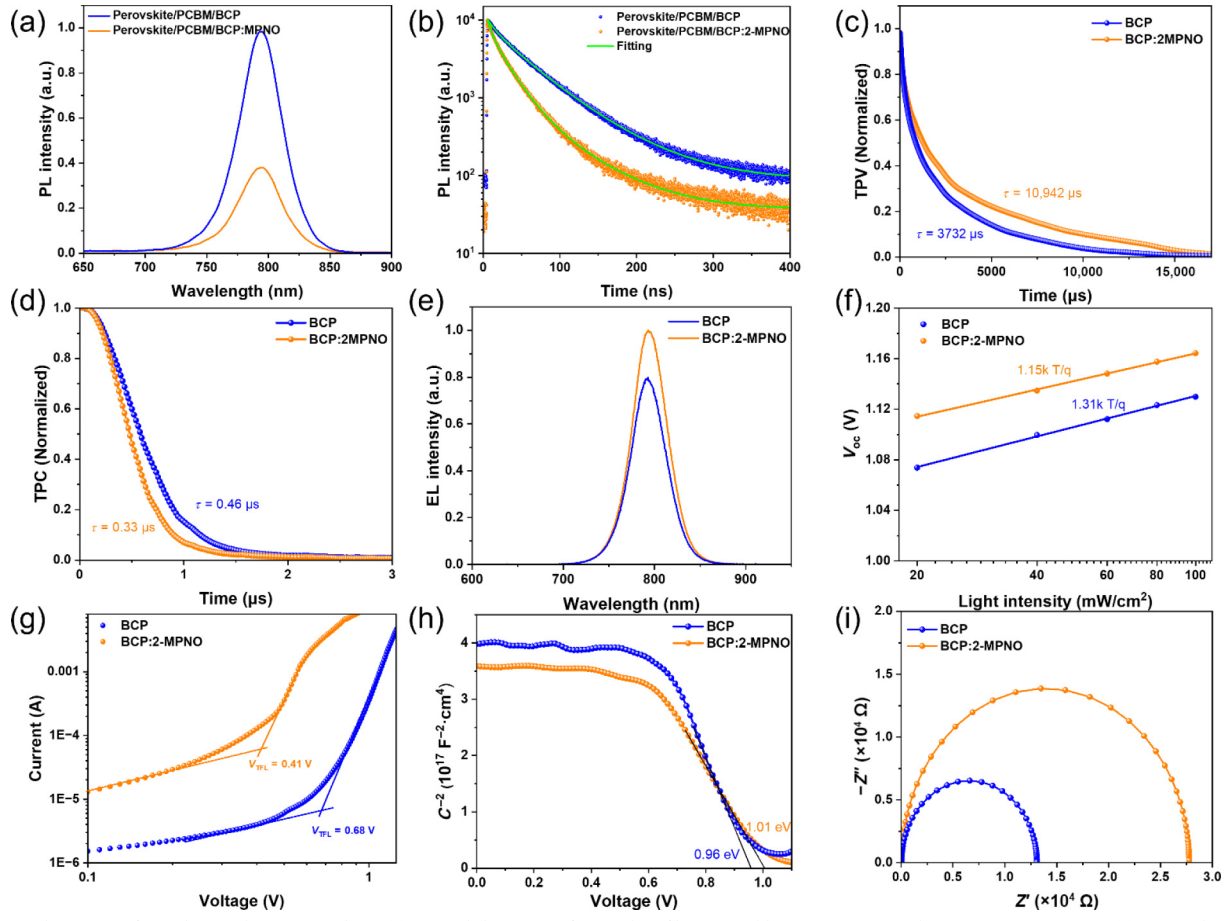

Figure 3 Charge transfer and recombination analysis. (a) PL and (b) TRPL of perovskite films coated by PCBM/BCP and PCBM/BCP:2-MPNO. (c) TPV, (d) TPC, (e) EL, and (f) V_{OC} versus light intensity of PSCs based on BCP and BCP:2-MPNO. (g) SCLC curves of the electron-only devices with structures of FTO/SnO_2/perovskite/PCBM/BCP:2-MPNO (or BCP)/Ag. (h) Mott–Schottky plots obtained at 100 Hz and (i) EIS of PSCs based on BCP and BCP:2-MPNO. Inset shows the equivalent circuit of the Nyquist plots.

parameters detailed in Table S5 in the ESM. For the BCP device, the series resistance (R_s) was measured at 37.19 Ω, with a recombination resistance (R_{rec}) of 1.31 × 10^4 Ω. In comparison, the BCP:2-MPNO device exhibited a reduced R_s of 34.25 Ω and an increased R_{rec} of 2.77 × 10^4 Ω. These changes in resistance values indicate that doping with 2-MPNO effectively suppresses interfacial recombination processes, thereby enhancing charge carrier separation and extraction efficiency within the device structure [35].

3.4 Interaction between 2-MPNO and Ag electrode

To elucidate the interaction between 2-MPNO and the Ag electrode, Raman spectroscopy was employed. Raman spectra were acquired by depositing a 5 nm Ag film onto a 2-MPNO layer. As illustrated in Fig. 4(a), the vibrational peaks observed at 711.08 and 1138.58 cm^{-1} correspond to the C–S single bond vibration of the thiol group and the N–O bond vibration within the 2-MPNO molecule, respectively [36]. After interaction with the Ag film, these peaks exhibited shifts to 695.21 and 1131.19 cm^{-1}, respectively, indicative of a chemical interaction between 2-MPNO and Ag.

Further analysis of the interaction between 2-MPNO and the Ag electrode was conducted using X-ray photoelectron spectroscopy (XPS), as presented in Figs. 4(b)–4(d). The observed splitting of the S 2p and O 1s peaks may be attributed to the tautomeric form of 2-MPNO, specifically hydroxyl-2-(1H)-pyridinethione [37]. Upon coordination with 2-MPNO, the Ag 3d peak exhibited a positive shift of approximately 0.32 eV in binding energy, whereas the S 2p and O 1s peaks of 2-MPNO shifted by −1.3 and +1.2 eV, respectively. These spectral shifts substantiate the presence of a strong interaction between 2-MPNO and the Ag electrode. This bidentate coordination not only enhances interfacial electronic coupling but also establishes a molecular-level diffusion barrier, effectively suppressing Ag^+ ion migration and thereby improving interfacial stability.

To assess the influence of 2-MPNO incorporation on the buried interface of the Ag electrode, 20 nm Ag films were deposited onto BCP and BCP:2-MPNO substrates, followed by AFM analysis. The three-dimensional (3D) AFM images are shown in Figs. 4(e) and 4(f), and the corresponding two-dimensional (2D) images are presented in Fig. S7 in the ESM. The robust interaction between 2-MPNO and Ag facilitated conformal growth of the Ag film, markedly reducing the grain size and yielding a denser morphology. Correspondingly, the surface roughness decreased from 1.80 to 1.71 nm. Such a smooth and conformal Ag film morphology is conducive to efficient electron extraction from the electron transport layer to the Ag electrode [38].

3.5 Elemental diffusion and device stability

To evaluate the impact of 2-MPNO doping on device stability, both storage and thermal stability tests were performed on unencapsulated devices. As shown in Fig. 5(a), the unencapsulated

BCP:2-MPNO-based device maintained 97.4% of its initial efficiency after being stored for 2115 h at 25 °C under ambient air conditions with 15% ± 5% relative humidity, indicating exceptional long-term stability. In contrast, the efficiency of the BCP-based device declined to 91.7% of its original value. Thermal stability results are presented in Fig. 5(b). Following thermal aging at 65 °C in a nitrogen atmosphere for 1256 h, the unencapsulated BCP:2-MPNO device demonstrated notable stability, retaining 94.0% of its initial efficiency. Conversely, the efficiency of the BCP device decreased to 87% of its initial level. These findings suggest that doping with 2-MPNO substantially enhances the stability of inverted PSCs. This improvement is attributed to the strong coordination interactions between the thiol groups and oxygen atoms in 2-MPNO molecules with the Ag electrode, which effectively inhibit Ag diffusion into the perovskite layer, thereby enhancing thermal stability [39].

To investigate elemental diffusion during the aging process, cross-sectional SEM and energy-dispersive X-ray (EDX) spectroscopy analyses were conducted. As depicted in Fig. 5(c), after thermal aging at 65 °C in a nitrogen atmosphere for 300 h, significant diffusion of Ag into the perovskite layer was observed in the BCP-based device, accompanied by iodine(I) diffusion into the Ag electrode. The migration of Ag accelerates chemical reactions between Ag and the perovskite, which likely constitutes the primary mechanism underlying the rapid performance degradation observed during aging. Simultaneously, the diffusion of I into the Ag electrode can lead to the formation of insulating silver AgI, impeding charge transport [40]. In contrast, in the 2-MPNO-doped device, robust interactions between 2-MPNO and the Ag electrode effectively suppressed Ag diffusion into the perovskite layer, thereby significantly improving the long-term stability of the device, as shown in Fig. 5(d). Figure S8 in the ESM presents the corresponding EDX line-scan across the interface, which more clearly illustrate the suppression of ion migration.

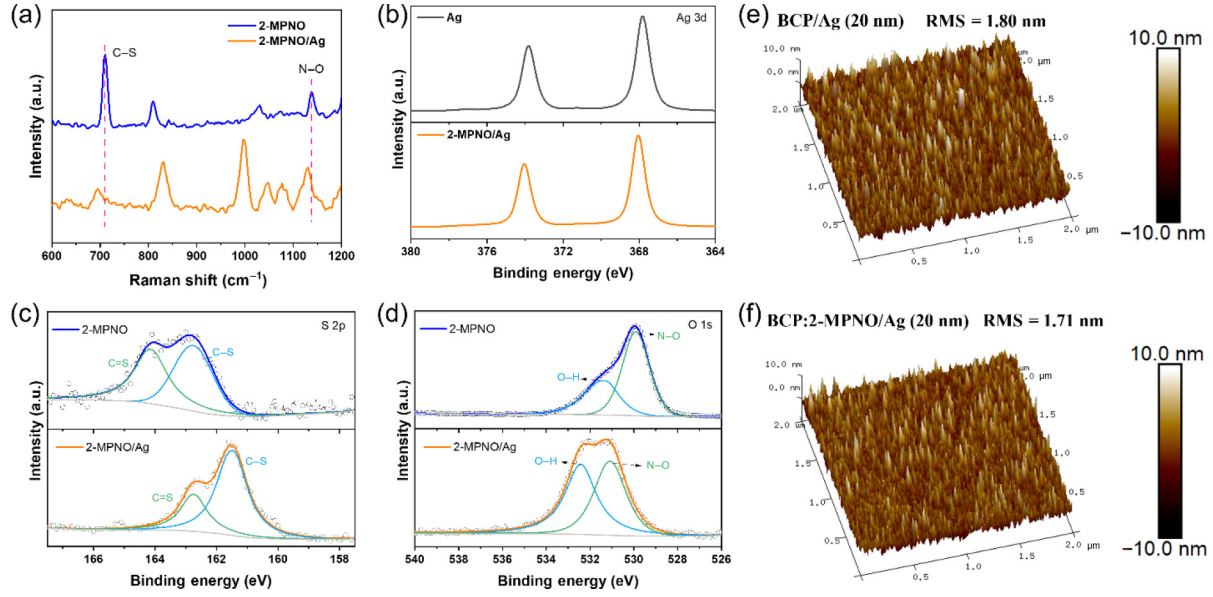

Figure 4 Interaction between 2-MPNO and Ag electrode. (a) Raman spectra. (b) Ag 3d, (c) S 2p, and (d) O 1s XPS spectra. 3D AFM images of (e) BCP/Ag (20 nm) and (f) BCP:2-MPNO/Ag (20 nm) deposited on ITO substrates.

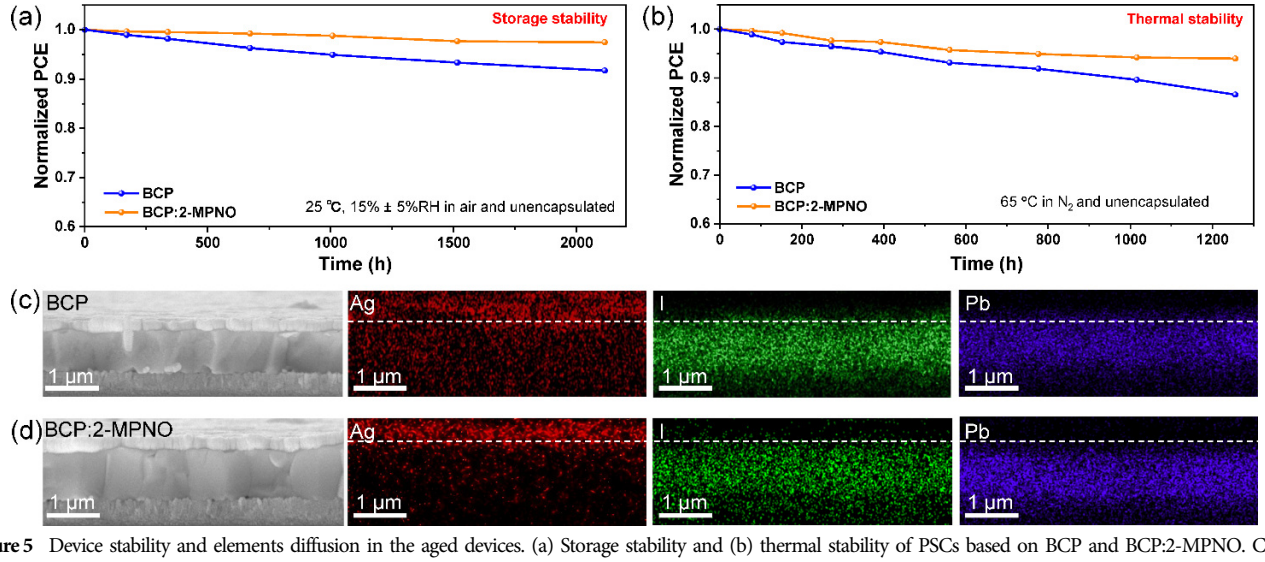

Figure 5 Device stability and elements diffusion in the aged devices. (a) Storage stability and (b) thermal stability of PSCs based on BCP and BCP:2-MPNO. Cross-sectional SEM and EDX mapping of Ag, I, and Pb in the aged devices based on (c) BCP and (d) BCP:2-MPNO.

4 Conclusions

Here we propose an effective strategy to simultaneously mitigate two critical issues including interfacial charge transport and metal diffusion that compromise the fabrication and long-term operation of PSCs under ambient conditions. This is realized through the molecular engineering by incorporating 2-MPNO into the BCP cathode buffer layer. The n-type doping properties of 2-MPNO substantially enhance the conductivity of BCP and optimize the energy level alignment at the PCBM/Ag interface by inducing an upward shift in the Fermi level, thereby facilitating improved electron mobility. Additionally, the thiol and N–O functional groups in 2-MPNO establish robust chemical bonds with Ag via a bidentate coordination mechanism, forming a molecular-scale diffusion barrier that effectively inhibits Ag electrode migration. This synergistic interaction enables the champion device to achieve a PCE of 25.31%, while maintaining 94.0% of its initial performance after 1256 h of thermal aging at 65 °C under nitrogen atmosphere. By innovatively integrating doping chemistry with coordination chemistry, this study introduces a novel paradigm for the design of multifunctional interfacial layers that concurrently promote efficient charge transport and mitigate electrode degradation, representing a significant advancement toward the industrial deployment of perovskite photovoltaic technologies.

Electronic Supplementary Material: Supplementary material (Figs. S1–S8 and Tables S1–S5 including the *J*–*V* characteristics, statistical distribution, absorption spectra, Tauc plots, photovoltaic parameters, AFM images, TOF-SIMS depth profile, EDX line scan, fitting parameters of the TRPL results, and EIS fitting parameters) is available in the online version of this article at https://doi.org/10.26599/NR.2026.94908437.

Data availability

All data needed to support the conclusions in the paper are presented in the manuscript and the Electronic Supplementary Material. Additional data related to this paper may be requested from the corresponding author upon request.

Acknowledgements

The authors would like to thank the National Natural Science Foundation of China (Nos. 62204222, 52321006, T2394480, and T2394484), the Natural Science Foundation of Henan (No. 262300421817), and the National Key R&D Program of China (No. 2023YFE0111500).

Declaration of competing interest

All the contributing authors report no conflict of interests in this work.

Author contribution statement

Z. Y. W.: Project administration, writing – original draft, experimental design, funding acquisition. Z. Q. L.: Data curation, validation, formal analysis. L. L.: Investigation. B. Z.: Investigation. M. Y. L.: Investigation. D. Y.: Supervision, writing – review & editing. Y. L. S.: Supervision, funding acquisition. All the authors have approved the final manuscript.

Use of AI statement

None.

References

[1] Green, M. A.; Dunlop, E. D.; Yoshita, M.; Kopidakis, N.; Bothe, K.; Siefer, G.; Hao, X. J.; Jiang, J. Y. Solar cell efficiency tables (version 66). *Prog. Photovoltaics: Res. Appl.* **2025**, *33*, 795–810.

[2] Xiong, Z.; Zhang, Q.; Cai, K.; Zhou, H. T.; Song, Q.; Han, Z. Y.; Kang, S. Q.; Li, Y. W.; Jiang, Q.; Zhang, X. W. et al. Homogenized chlorine distribution for > 27% power conversion efficiency in perovskite solar cells. *Science* **2025**, *390*, 638–642.

[3] Liu, L.; Farhadi, B.; Li, J. X.; Liu, S. Y.; Lu, L. F.; Wang, H.; Du, M. Y.; Yang, L. Y.; Bao, S. J.; Jiang, X. et al. Hydrophobic hydrogen-bonded polymer network for efficient and stable perovskite/Si tandem solar cells. *Angew. Chem., Int. Ed.* **2024**, *63*, e202317972.

[4] Chin, X. Y.; Turkay, D.; Steele, J. A.; Tabean, S.; Eswara, S.; Mensi, M.; Fiala, P.; Wolff, C. M.; Paracchino, A.; Artuk, K. et al. Interface passivation for 31.25%-efficient perovskite/silicon tandem solar cells. *Science* **2023**, *381*, 59–63.

[5] Zhang, X.; Ma, Q. Y.; Wang, Y. S.; Zheng, J. Z.; Liu, Q. X.; Liu, L. M.; Yang, P.; He, W. J.; Cao, Y.; Duan, W. Y. et al. Ligand homogenized Br–I wide-bandgap perovskites for efficient NiO_x-based inverted semitransparent and tandem solar cells. *ACS Nano* **2024**, *18*, 15991–16001.

[6] Li, H.; Yan, Z.; Li, M.; Wen, X. Y.; Deng, S.; Liu, S. S.; Choy, W. C. H.; Li, L. J.; Li, M. Y.; Lu, H. F. Probing the stability of perovskite solar cell under working condition through an ultra-thin silver electrode: Beyond the halide ion diffusion and metal diffusion. *Chem. Eng. J.* **2023**, *458*, 141405.

[7] Jiang, C. F.; Zhou, J. J.; Li, H.; Tan, L. G.; Li, M. H.; Tress, W.; Ding, L. M.; Grätzel, M.; Yi, C. Y. Double layer composite electrode strategy for efficient perovskite solar cells with excellent reverse-bias stability. *Nano-Micro Lett.* **2023**, *15*, 12.

[8] Li, H.; Xie, G. S.; Fang, J.; Wang, X.; Li, S. B.; Lin, D. X.; Wang, D. Z.; Huang, N. S.; Peng, H. C.; Qiu, L. B. Holistic dielectric and buffer interfacial layers enable high-efficiency perovskite solar cells and modules. *Nano Energy* **2024**, *124*, 109507.

[9] Lee, K.; Ryu, J.; Yu, H.; Yun, J.; Lee, J.; Jang, J. Enhanced efficiency and air-stability of NiO_x-based perovskite solar cells via PCBM electron transport layer modification with Triton X-100. *Nanoscale* **2017**, *9*, 16249–16255.

[10] Zhuang, J.; Wang, J. Z.; Yan, F. Review on chemical stability of lead halide perovskite solar cells. *Nano-Micro Lett.* **2023**, *15*, 84.

[11] Svanström, S.; Jacobsson, T. J.; Boschloo, G.; Johansson, E. M. J.; Rensmo, H.; Cappel, U. B. Degradation mechanism of silver metal deposited on lead halide perovskites. *ACS Appl. Mater. Interfaces* **2020**, *12*, 7212–7221.

[12] Li, X.; Ding, H. H.; Li, G. H.; Wang, Y.; Fang, Z. M.; Yang, S. F.; Ju, H. X.; Zhu, J. F. *In situ* investigations of interfacial degradation and ion migration at $CH_3NH_3PbI_3$ perovskite/Ag interface. *Chin. J. Chem. Phys.* **2019**, *32*, 299–305.

[13] Ming, W. M.; Yang, D. W.; Li, T. S.; Zhang, L. J.; Du, M. H. Formation and diffusion of metal impurities in perovskite solar cell material $CH_3NH_3PbI_3$: Implications on solar cell degradation and choice of electrode. *Adv. Sci.* **2018**, *5*, 1700662.

[14] Liang, Z. Q.; Ren, Z. Q.; Wang, Z. Y.; Yan, N.; Li, L.; Zhang, B.; Song, Y. L. Boosting charge extraction and efficiency of inverted perovskite solar cells through coordinating group modification at the buffer layer/cathode interface. *Nano Res.* **2025**, *18*, 94907075.

[15] Chen, P.; Xiao, Y.; Hu, J. T.; Li, S. D.; Luo, D. Y.; Su, R.; Caprioglio, P.; Kaienburg, P.; Jia, X. H.; Chen, N. et al. Multifunctional ytterbium oxide buffer for perovskite solar cells. *Nature* **2024**, *625*, 516–522.

[16] Liu, N. H.; Xiong, J.; Wang, G.; He, Z.; Dai, J. Q.; Zhang, Y. S.; Huang, Y.; Zhang, Z. L.; Wang, D. J.; Li, S. et al. Overcoming the

PCBM/Ag interface issues in inverted perovskite solar cells by rhodamine-functionalized dodecahydro-*closo*-dodecaborate derivate interlayer. *Adv. Funct. Mater.* **2023**, *33*, 2300396.

[17] Castro-Hermosa, S.; Wouk, L.; Bicalho, I. S.; de Queiroz Corrêa, L.; de Jong, B.; Cinà, L.; Brown, T. M.; Bagnis, D. Efficient fully blade-coated perovskite solar cells in air with nanometer-thick bathocuproine buffer layer. *Nano Res.* **2021**, *14*, 1034–1042.

[18] Dong, X.; Fang, X.; Lv, M. H.; Lin, B. C.; Zhang, S.; Ding, J. N.; Yuan, N. Y. Improvement of the humidity stability of organic-inorganic perovskite solar cells using ultrathin Al_2O_3 layers prepared by atomic layer deposition. *J. Mater. Chem. A* **2015**, *3*, 5360–5367.

[19] Kim, I. S.; Cao, D. H.; Buchholz, D. B.; Emery, J. D.; Farha, O. K.; Hupp, J. T.; Kanatzidis, M. G.; Martinson, A. B. F. Liquid water- and heat-resistant hybrid perovskite photovoltaics via an inverted ALD oxide electron extraction layer design. *Nano Lett.* **2016**, *16*, 7786–7790.

[20] Zhang, X. W.; Liang, C. J.; Sun, M. J.; Zhang, H. M.; Ji, C.; Guo, Z. B.; Xu, Y. J.; Sun, F. L.; Song, Q.; He, Z. Q. Improved fill factor in inverted planar perovskite solar cells with zirconium acetate as the hole-and-ion-blocking layer. *Phys. Chem. Chem. Phys.* **2018**, *20*, 7395–7400.

[21] Wu, Y. L.; Wan, L.; Fu, S.; Zhang, W. X.; Li, X. D.; Fang, J. F. Liquid metal acetate assisted preparation of high-efficiency and stable inverted perovskite solar cells. *J. Mater. Chem. A* **2019**, *7*, 14136–14144.

[22] Liu, A. C.; Li, X. D.; Zhang, W. X.; Yang, H.; Guo, X. M.; Lu, C. Y.; Yuan, H. B.; Ou-Yang, W.; Fang, J. F. Ag electrode anticorrosion in inverted perovskite solar cells. *Adv. Funct. Mater.* **2024**, *34*, 2307310.

[23] Li, X. D.; Fu, S.; Zhang, W. X.; Ke, S. Z.; Song, W. J.; Fang, J. F. Chemical anti-corrosion strategy for stable inverted perovskite solar cells. *Sci. Adv.* **2020**, *6*, eabd1580.

[24] Yang, J. B.; Cao, Q.; Wang, T.; Yang, B. W.; Pu, X. Y.; Zhang, Y. X.; Chen, H.; Tojiboyev, I.; Li, Y. K.; Etgar, L. et al. Inhibiting metal-inward diffusion-induced degradation through strong chemical coordination toward stable and efficient inverted perovskite solar cells. *Energy Environ. Sci.* **2022**, *15*, 2154–2163.

[25] Li, Y. H.; He, X. L.; Zhu, R. Q.; Chen, X. Y.; Wang, T.; Pu, X. Y.; Chen, H.; Cao, Q.; Li, X. H. Enhanced corrosion resistance of Ag electrode through ionized 2-mercaptobenzothiazole in inverted perovskite solar cells. *Adv. Funct. Mater.* **2025**, *35*, 2413245.

[26] Chiang, S. E.; Chandel, A.; Thakur, D.; Chen, Y. T.; Lin, P. C.; Wu, J. R.; Cai, K. B.; Kassou, S.; Yeh, J. M.; Yuan, C. T. et al. On the role of solution-processed bathocuproine in high-efficiency inverted perovskite solar cells. *Sol. Energy* **2021**, *218*, 142–149.

[27] Yang, D.; Zhou, X.; Yang, R. X.; Yang, Z.; Yu, W.; Wang, X. L.; Li, C.; Liu, S. Z.; Chang, R. P. H. Surface optimization to eliminate hysteresis for record efficiency planar perovskite solar cells. *Energy Environ. Sci.* **2016**, *9*, 3071–3078.

[28] Yang, D.; Yang, R. X.; Wang, K.; Wu, C. C.; Zhu, X. J.; Feng, J. S.; Ren, X. D.; Fang, G. J.; Priya, S.; Liu, S. Z. High efficiency planar-type perovskite solar cells with negligible hysteresis using EDTA-complexed SnO_2. *Nat. Commun.* **2018**, *9*, 3239.

[29] Tuo, B. Y.; Wang, Z. Y.; Ren, Z. Q.; Zhang, H. W.; Lu, X. Q.; Zhang, Y. Q.; Zang, S. Q.; Song, Y. L. A novel radical-reaction interruption strategy for enhancing the light stability of perovskite solar cells. *Energy Environ. Sci.* **2024**, *17*, 2945–2955.

[30] Yan, N.; Cao, Y.; Jin, Z. W.; Liu, Y. C.; Liu, S. Z.; Fang, Z. M.; Feng, J. S. Surface reconstruction for efficient NiO_x-based inverted perovskite solar cells. *Adv. Mater.* **2024**, *36*, 2403682.

[31] Liu, Y. H.; Zhao, Y. M.; Han, J. D.; Sun, X. L.; Yang, H. H.; Huang, Z.; Yan, H.; Zhang, M.; Zhang, S. S.; Zhang, Y. Q. et al. Metal-organic-framework-assisted inhibition of interface oxygen migration for exceptional thermal stability of perovskite solar cells. *Nano Res.* **2025**, *18*, 94907685.

[32] Elumalai, N. K.; Uddin, A. Open circuit voltage of organic solar cells: An in-depth review. *Energy Environ. Sci.* **2016**, *9*, 391–410.

[33] Zheng, L. F.; Shen, L. N.; Xu, P.; Huang, Y.; Li, F. Y.; Yang, J. X.; Tian, C. B.; Xie, L. Q.; Wei, Z. H. Surface termination of perovskite with 1-naphthylmethylammonium tetrafluoroborate for efficient perovskite solar cells. *Nano Res.* **2025**, *18*, 94907319.

[34] Cao, Y.; Feng, J. S.; Wang, M. Z.; Yan, N.; Lou, J. J.; Feng, X. L.; Xiao, F. W.; Liu, Y. C.; Qi, D. Y.; Yuan, Y. et al. Interface modification by ammonium sulfamate for high-efficiency and stable perovskite solar cells. *Adv. Energy Mater.* **2023**, *13*, 2302103.

[35] Wang, Z. Y.; Zhu, X. J.; Feng, J. S.; Wang, C. Y.; Zhang, C.; Ren, X. D.; Priya, S.; Liu, S. Z.; Yang, D. Antisolvent- and annealing-free deposition for highly stable efficient perovskite solar cells via modified ZnO. *Adv. Sci.* **2021**, *8*, 2002860.

[36] Niu, D. Z.; Mu, L. L.; Lu, Z. S.; Song, B. L.; Sun, B. W. Synthesis and crystal structure of $Pr(mpo)_3(DMSO)_2$ (Hmpo = 2-mercaptopyridine N-oxide). *J. Chem. Crystallogr.* **2004**, *34*, 195–198.

[37] Butler, M.; Cabrera, G. M. A mass spectrometry and DFT study of pyrithione complexes with transition metals in the gas phase. *J. Mass Spectrom.* **2017**, *52*, 728–738.

[38] Chakravarthi, N.; Gunasekar, K.; Cho, W.; Long, D. X.; Kim, Y. H.; Song, C. E.; Lee, J. C.; Facchetti, A.; Song, M.; Noh, Y. Y. et al. A simple structured and efficient triazine-based molecule as an interfacial layer for high performance organic electronics. *Energy Environ. Sci.* **2016**, *9*, 2595–2602.

[39] Yu, B.; Wang, K.; Sun, Y. P.; Yu, H. Z. Multi-functional interface modulation through thiol functionalized covalent organic frameworks for efficient and durable perovskite solar cells. *J. Mater. Chem. A* **2024**, *12*, 27577–27587.

[40] Li, J. W.; Dong, Q. S.; Li, N.; Wang, L. D. Direct evidence of ion diffusion for the silver-electrode-induced thermal degradation of inverted perovskite solar cells. *Adv. Energy Mater.* **2017**, *7*, 1602922.